Draft

Surfaces with bent micro-polymerized pillars exhibit enhanced heat transfer during subcooled flow boiling

Wei-Ting Hsu*, Namkyu Lee†, Donghwi Lee#, JeongJu Kim*, and Hyung Hee Cho*,‡

* Department of Mechanical Engineering, Yonsei University, 50 Yonsei-ro, Seodaemun-gu, Seoul 120-749, Korea

†ICS-3 Soft Condensed Matter, Forschungszentrum Jülich GmbH, D-52428 Jülich, Germany

#Department of Mechanical Engineering, University of Wisconsin–Madison, 1500 Engineering Drive, Madison, WI 53706, United States

‡Corresponding author: hhcho@yonsei.ac.kr (H. H. Cho)

Abstract

Anisotropic wicking surfaces reveal a unique liquid-spreading behavior with directional dependence. By manipulating the bending direction of polymerized pillars with tilting angles of the pillars, surfaces composed of the anisotropic wicking structures strengthen capillary driving forces along the preferred direction. In the present work, we created surfaces composed of the bending-polymerized pillar arrays with a 250 um and 500 um center-to-center spacing to experimentally determine the influence of the anisotropic wicking surfaces on flow boiling heat transfer under subcooled conditions compared to those vertical-polymerized pillar surface. The vertical-polymerized pillars were deflected with an averaged tilting angle of 30° by conducting a bending treatment on the polymerized pillar surface. Various test surfaces related to the surface wettability were manipulated to evaluate the effect of wicking characteristics on boiling heat transfer under subcooled flow conditions.

A notable enhancement in the critical heat flux (17-34%) and the heat transfer coefficient (32-71%) on the polymerized pillar surfaces was observed compared to bare polymerized surfaces, respectively; meanwhile, narrowing the spacings between polymerized pillars resulted in an increasing trend in boiling heat transfer under subcooled-convective flow. The anisotropic surfaces significantly improved the wicking- and the boiling heat transfer characteristics compared to surfaces with vertical-polymerized pillars. These experimental results were further demonstrated by theoretically analyzing the relationship between the liquid pinning force and the design layout of the polymerized-pillar surfaces to better approach the enhancement mechanisms of the anisotropic wicking surfaces in subcooled flow boiling.

Keywords:

Subcooled flow boiling heat transfer; Anisotropic wicking surface; Bending-polymerized pillar arrays; Bubble visualization

Nomenclature

A	=	Heated area (m^2)
D	=	Departure diameter (mm)
F_p	=	Pinning force of liquid (N)
h	=	Heat transfer coefficient ($W/m^2 \cdot K$)
I	=	Imported current (A)
k	=	Thermal conductivity (W/m·K)
L	=	Length (m)
l	=	Wicking distance (mm)
Q	=	Total input heat (W)
q	=	Heat flux (W/m^2)
q_{loss}	=	Heat loss (W/m^2)
Re	=	Reynolds number
P	=	Center-to-center spacing between polymerized pillars (mm)
T	=	Temperature (°C)
t	=	Time (s)
V	=	Voltage drop of the ITO heater (V)
Greek letter		
α	=	Advancing contact angle (°)
β	=	Receding contact angle (°)
γ	=	Radius of the contact line
θ	=	Static contact angle (°)
$\Delta\theta$	=	Contact angle hysteresis
σ	=	Surface tension (N/m)
δ	=	Thickness of RTD sensor (m)
ε	=	Standard deviation

Subscripts

b	=	Bubble
c	=	Contact
e	=	Entrance
f	=	Fluid
h	=	Hydraulic
R	=	RTD sensor
si	=	Silicon
W	=	Heated wall

1. Introduction

Over the past few decades, as the development of fuel cell technology become mature, automobiles in the city transportation networks have been gradually replaced by battery electric vehicles, such as an electric vehicle (EV), battery electric vehicle (BEV), and plug-in hybrid electric vehicle (PHEV), etc., which are mainly or partially motor by electric power of fuel cells [1]. In general, heat flux generated by EV power systems comprised of IC packages is predicted above 300 W/cm^2, which cannot be efficiently transferred into the relative operating environment using common cooling mechanisms in terms of nature- and forced- convection using gas or liquid, respectively. Therefore, the actual working temperature of the EV power system should be maintained below 200 °C to reduce power loss and prevent the circuit parts from malfunctioning [2].

Boiling heat transfer is a highly efficient cooling method for high power units by inducing vapor bubbles to transport latent heat with phase change phenomena, however, applying such a mechanism with high heat dissipation capacities to electronic devices still face difficulties concerning limitations of boiling crisis and flow instability [3-4]. In terms of the critical point of boiling heat transfer, which is also called critical heat flux (CHF), heat transfer on a target will be exhibited as a premature dry-out occur where the entire surface is covered by a vapor film preventing coolant from reaching the heated surface, therefore deteriorate the overall boiling heat transfer performance. In contrast, the boiling crisis will occur untimely as the intensity of flow instability increase; even though the heat energy can be frequently removed through bubble-occurred perturbation within the superheated liquid layer, a significant flow oscillation will occur as a result in mechanical vibration within working chambers as the bubble nucleation become vigorous, especially within a relatively large heat flux regime [5], therefore resulting in a premature CHF.

However, these detrimental effects on boiling heat transfer can be suppressed by constructing artificial-roughened structures on heated surfaces for improving surface coolant-supply ability; despite manipulating surface wettability via chemical electrodeposition [6-7], using surfaces consisted of micro/nanopillar arrays to enhance heat transfer area, as well as interfacial wicking characteristics, are a common strategy for achieving high boiling heat transfer performance [8-9]. As for the influence of surfaces composed of nanopillar arrays on boiling heat transfer, Chen et al. [8] experimentally investigate the effect of random-aligned nanopillars, made by Cu or Si, on pool boiling heat transfer at saturated conditions, respectively;

a remarkable enhancement in both heat transfer coefficient (HTC) and CHF was observed as compared to bare silicon surfaces, by 100%, which was attributed to high interfacial wicking capacities offered by the nano-structuring surfaces. In addition to improving coolant-supply ability, surfaces comprised of nanopillar arrays can also improve the thermal stability on heated surfaces in pool and flow boiling [10-11].

On the other hand, surfaces composed of nanopillar arrays can also enhance the overall boiling heat transfer under flow boiling conditions by improving the capillary driving forces in microchannels [12-14], respectively. While vapor bubbles may trap by the roughened surface along the flow direction in flow boiling, Li et al. [13] experimentally investigated the influence of surfaces composed of silicon nanowires with various mass flow rates on subcooled flow boiling heat transfer. According to their experimental results, the heat dissipation capacity in HTC on the nanowire coated surface was significantly lower than the silicon-surface microchannel, which was attributed to the relatively high evaporation rate against the liquid repellent capacity on surfaces composed of nanowires. In other words, it was conjectured that the expending vapor was trapped by the nanowire coated surfaces because the roughened surface fabricated by nanopillar arrays was not only enhancing the interfacial wicking characteristics but also increasing the pinning force of bubbles, thereby resulted in a decreasing trend in the boiling heat transfer [15].

Several studies were experimentally conducted on surfaces composed of micropillar arrays for determining its influence on boiling heat transfer in forced convective flow to diminish the presence of pinning force of vapor bubbles on the roughened surface with nanowires, especially in the annular flow regime, which dominated the film evaporation performance [16-17]. Zhu et al. [17] created vertical-aligned micropillar arrays with silicon materials in a microchannel based on a standard etching process; they found that the microchannel synthesized with micropillar arrays revealed a relatively stable surface temperature distribution with a uniform liquid film covered on micropillar surfaces compared to the smooth surface, indicating that the micropillar arrays were able to induce capillary wicking to maintain thin film evaporation. Therefore, surfaces composed of micropillar arrays should be selected as the promising structure for enhancing the overall flow boiling heat transfer, owing to its high wicking behavior with the relatively low viscous resistance compared to those comprised of nanopillar arrays.

Additionally, the interfacial wicking intensity can be further increased in preferred directions by anisotropic wicking structures. When one side of micro- or nano- pillars are

deposited with a thin metal film, residual stresses will remain within the interfacial surface between the pillar arrays and the metal coating layers allowing micro- /nano- pillars to deflect at a certain angle, i.e., the deflected angle of pillars are strongly dominated by the depositing thickness of metal coated layers [18-19]. By conducting the bending treatment on pillar arrays, liquid on surfaces composed of bending pillar arrays can be driven directional along the pillar tilting direction [20-21]. Therefore, a significant enhancement in boiling heat transfer in forced convective flow can be expected utilizing surfaces with micro-bending pillars to further intensify the liquid driving force on surfaces along the flow direction, owing to the directional dependence of the wicking behavior of the pillar arrays. Notably, the influence of the bending pillar arrays in terms of the nature of liquid anisotropy on subcooled flow boiling heat transfer has still not been experimentally evaluated.

Accordingly, we controlled the surface wettability by coating a uniform hydrophilic layer on test surfaces, and fabricated surfaces consisted of micro-polymerized pillar arrays on silicon substrates with variation in the center-to-center spacing between pillar arrays. The polymerized pillar arrays were fabricated on the silicon substrates with vertical- and bending- alignments, respectively, as shown in Fig. 1. The effect of the anisotropic wicking structures on boiling heat transfer under subcooled flow conditions related to the bending effect of wettability micro-polymerized pillars, i.e., vertical- and bending- pillar arrays coating with and without hydrophilic coated layers, with different center-to-center spacings, were experimentally examined; in particular, the relationship between liquid pinning forces of the bending pillar arrays on boiling heat transfer characteristics under subcooled conditions was also analyzed in the present work.

2. Experimental method

2.1 Experimental equipment and procedure

The influence of the anisotropic wicking of the polymerized micropillar surfaces under subcooled flow boiling conditions was evaluated in the present work. The detailed information concerning the experimental setup is schematically showed in Fig. 2(a). We used deionized water as the working fluid and maintained at 100°C by a constant temperature base with an immersion heater for 2 hours to remove the residual air/gas before the heat transfer experiment; subsequently, a full-filled water storage tank with a capacity of 44 L storing degassed liquid where the pressure conditions were regulated using a pressure valve located atop the tank, was

used to provide the working fluid. A magnetic pump composed of an electric motor was used to continuously circulate the working fluid from the main reservoir into a test section passing through a heat exchanger and a flowmeter within the closed system. The heat exchanger was used to regulate the inlet temperature of the working fluid at 59.3 ±0.4 °C throughout the experiment. Additionally, the test section was designed with a rectangular channel where the width and height are 5 mm related to D_h = 5 mm, fabricating by polyetheretherketone (PEEK, k = 0.25 W/m-K); the entrance length of the flow channel (L_e) was adequate for achieving a fully developed flow, where the mass flow rate was maintained at 0.51 kg/min, (i.e., Re = 3600), and the required length was 86.13 mm following the design criterion of $4.4 \cdot Re^{1/6} \cdot D_h$.

Furthermore, the bubble visualization regions were located at the side of the flow chamber, created using two quartz windows, observing bubble characteristics on polymerized test surfaces in subcooled flow boiling. Two copper bus bars installed below test plates were connected to a direct current (DC) power supply, which imparted different rated powers to heat test surfaces. A silver paste with high conductivity (resistivity 10^{-4} Ω-cm) was utilized to diminish the resistance of interfacial surfaces between the heater electrodes and the copper bus bars, as shown in Fig. 2(b).

Moreover, the inlet and the outlet temperature of the working fluid was detected by K-type thermal couples at the flow chamber, and the surface temperature of test surfaces was measured via resistance temperature detector sensors (RTDs) [22-24]; these temperature measured components were connected to the data acquisition system consisted of a data recorder and a desktop to collect and examine experimental data as the temperature variation within 0.2 °C for 15 minutes. The design layout of RTDs used to detect the surface temperature in this study was schematically showed in Fig. 2(c). The detailed information related to experimental facilities in the present study can be found in our previous work [24], accordingly.

2.2 Fabrication process and bending treatment on vertical-polymerized pillar arrays

The fabrication process of the surface consisted of polymerized pillar arrays on silicon (Si) substrates is given in Fig. 3(a). Firstly, we used standard photolithography and reactive ion etching processes to create silicon molds with various circular cavities, i.e., 50 um in diameter and 300 um in-depth, which were etched vertically with 250-um and 500-um center-to-center spacings, respectively. The silicon molds were uniformly coated with 200-nm polydimethylsiloxane (PDMS) release agent (parylene C) using a parylene coater (KIST, Seoul, Korea) for reducing the affinity between the PDMS and silicon molds; the PDMS

solution with a mixed ratio of 10:1 was then poured on the silicon mold and cured at 80 °C for 8 hours in a conventional oven. After cross-linked the PDMS surface, PDMS stamps were peeled from the silicon mold following by coating the 200-nm parylene C layer; the prepared PDMS solution was subsequently poured onto the PDMS stamp, and a sharp scalpel was carefully used to remove the excess parts of PDMS. Based on a standard replica modeling method [25-26], the polymerized test surfaces were fabricated by vertically attached the PDMS stamp comprised of pillar arrays on a silicon substrate within the curing process for 8 hours, as shown in Fig. 3(b); by removing the PDMS stamp from the silicon substrate, surfaces composed of vertical-polymerized pillar arrays with 250-um and 500-um center-to-center spacings were created, respectively, as shown in Fig. 3(c). In addition, the area of the polymerized pillar surfaces was equivalent to the heated area, where the width and length were 5 mm and 10 mm, respectively. A bending treatment was conducted on the vertical PDMS pillar arrays by deflecting the pillars with an averaged angle of 30° with coating a thin gold layer, i.e., 200-um for hydrophilic- and 220-um for hydrophobic- surfaces, using a sputter coater, the further information related to the pillar bending process is given in the supplementary materials. Therefore, surfaces consisted of bending PDMS pillar arrays and silicon substrates were fabricated, resulting a considerable wicking behavior with directional dependence, i.e., so-called *unidirectional wicking* structures [20].

Fig. 4(a) shows the thickness of multi-coating layers on the surfaces consisted of vertical- and bending-polymerized pillar arrays and Si-substrates, respectively. A 200-nm SiO_2 was uniformly coated on the pillar arrays for further enhancing the capillary driving force on test surfaces; on the other hand, additional 20-nm gold coating layers were coated on the surfaces composed of polymerized pillar arrays using an e-beam evaporator (KIST, South, Korea) ensuring that the surfaces were created homogeneously, as shown in Fig. 4(b). In addition, the thickness of surfaces comprised of the multi-coating layers was confirmed using a scanning electron microscope, a hydrophilic test surface composed of bending pillar arrays with 500-um center-to-center spacing was selected as the representative case; notably, a 200-nm PDMS membrane was maintained at the interfacial surface between the gold coating layer and the Si substrate, as shown in Fig. 4(c). The configurations of the various test surfaces are summarized in Table 1.

2.3 Surface wettability on test surfaces

Surface wettability related to the measured surface contact angle (CA, θ_c) on test surfaces

is shown in Fig. 5(a), measured by a contact angle goniometer measurement; among the hydrophobic test surfaces, surfaces composed of polymerized pillar arrays with 250-um center-to-center spacing revealed the highest apparent surface CA, which can be referred to as the relatively large amount of air volume trapped by the liquid droplet resulting in highest surface hydrophobicity than the other comparisons. In contrast, when the polymerized test surfaces were coated with hydrophilic coating layers, the hydrophobic surfaces changed into hydrophilic surfaces comprising bending pillar arrays with 250-um center-to-center spacing showed the highest surface hydrophilicity compared with the other test surfaces. These measurement results related to the CA on test surfaces are in a well-agreement with the Wenzel state [27] and the Cassie-Baxter stare [28], considering with the roughness factor, respectively, i.e., the surface hydrophilicity increased as the roughness factor increased; the surface hydrophobicity intensified as the trapped air volume increased, as shown in Fig. 5(b). Interestingly, the surface composed of bending pillar arrays with the same center-to-center spacing between two neighboring pillars, either the hydrophilic or hydrophobic surfaces showed a decreasing trend in surface CA compared to those surfaces with vertical pillar arrays, which indicated that the surface wettability could be improved by deflection of the pillar arrays.

A similar trend of the surface CA on the anisotropic wicking structures can be found in previous works [19][29].

2.4 Data reduction related to boiling heat transfer characteristics

The heat flux applied on test surfaces q", is defined as follows:

$$q^{"} = \frac{\dot{Q}}{A} = \frac{V \times I}{A} \quad (1)$$

where $q^{"}$ is the applied heat flux, A is the heating area, V is the voltage drop from ITO heater, and I is the imported current. In addition, the surface temperature (T_w) was determined by the RTDs, which are composed of 5-measured points for detecting the wall temperature of the heated area, i.e., the width and the length were 5 mm and 10 mm, respectively. The calibration process of several points of the RTD sensor and the detailed information for CHF estimation can be found in our previous works [22-24]. The heated surface of the polymerized test surfaces was on the opposite side of the RTDs, the substrate thickness of the Si-plain was 550 um. Hence, the influence of the test plate' conduction was needed to determine the surface temperature based on one-dimensional thermal conduction [23-24].

$$q^{"} = (\frac{k_{si}}{l}) \times (T_R - T_w) \quad (2)$$

where k_{si} and l are the thermal conductivity and the substrate thickness of the Si plain, while T_R and T_w represent the temperature measured by the RTDs and the temperature of the heated wall, respectively.

In addition, Newton's law of cooling was used to estimate the heat dissipation capacity related to local heat transfer coefficient (HTC) of the various polymerized test surfaces, which is given by

$$q^{"} = h \times (T_w - T_f) \quad (3)$$

where h is the heat transfer coefficient of test surfaces, T_w and T_f are the wall temperature determined from Eq. (2), and the averaged bulk temperature of the working fluid at the inlet and outlet of the flow chamber.

2.5 Uncertainty analysis

The uncertainties of the experimental variables in the present work are summarized in Table 2., which were evaluated based on the method proposed by Moffat [30]. Accordingly, the dimension error of the length of patterns on the RTDs and the working temperature of the degassed DI water detecting by the thermocouple at the inlet and outlet of the flow chamber was $\pm 0.054\%$ and $\pm 0.22\%$, respectively. The measured temperature was taken into consideration by estimating the error of fluid property. Propagation of the uncertainties from the hydraulic diameter of the rectangular flow channel and the flow velocity of the working fluid resulted in uncertainty in Re of 4.56%.

A commercial CFD code (ANSUS, version 6.3.26) was utilized to evaluate the heat flux throughout the polymerized test surfaces was estimated to be 6.34% by assuming that the adequate heat spreading area corresponded to the convective heat transfer area, which. Therefore, we used the estimated-convective heat loss to evaluate the uncertainty of heat flux, determined by

$$\frac{\delta q''}{q''} = \left[\left(\frac{\delta V}{V}\right)^2 + \left(\frac{\delta I}{I}\right)^2 + \left(\frac{\delta A}{A}\right)^2 + (q_{loss})^2\right]^{\frac{1}{2}} \quad (4)$$

where the voltage-drop from the heater (V), the imported current (I), and the heating area (A) of the RTDs were utilized to calculate the relative heat flux uncertainty, which was 6.37 %. On the other hand, the uncertainty related to the heat transfer coefficient is determined by

$$\frac{\delta h}{h} = \left[\left(\frac{\delta q''}{q''}\right)^2 + \left(\frac{\delta T_f}{T_f}\right)^2 + \left(\frac{\delta T_w}{T_w}\right)^2\right]^{\frac{1}{2}} \quad (5)$$

Accordingly, the uncertainty of the heat transfer coefficient was evaluated to be 9.1% by substituting the uncertainties of the heat flux, the temperature of the working fluid, and the local wall temperature into Eq. (5)

Finally, the uncertainty of Reynolds number (Re), the heat flux, the HTC, and the local wall temperature was determined to be 4.56%, 6.37%, 9.1%, and 6.46%, respectively. The pixel uncertainty in the equilibrium diameter of a single departing bubble, which was determined via the bubble visualization, was ±0.1 mm [23-24].

3. Results and discussion

3.1 Anisotropic wicking surfaces in forced convective boiling heat transfer under subcooled conditions

Fig. 6 shows the subcooled flow boiling characteristics of the various hydrophilic- and hydrophobic-test surfaces used to analyze the relation between the degrees of subcooling and the relative heat flux with a Re value of 3600. Herein, surfaces with a 200-nm PDMS coating layer were selected as the reference surface compared to those surfaces composed of PDMS pillar arrays for determining the influence of the anisotropic wicking surfaces on subcooled flow boiling. Among the hydrophilic test surfaces, surfaces composed of PDMS pillar arrays showed a significant enhancement of CHF (217-248 W/cm^2) compared to the bare PDMS surface (185 W/cm^2). Herein, the surface with the PDMS pillars with narrow spacing (250 um) resulted in the highest boiling heat transfer compared to the other comparisons, as shown in Fig. 6(a). In addition, the bending effect of polymerized pillar surfaces was observed compared to the surfaces composed of vertical pillar arrays with the same center-to-center spacing that the CHF was further improved by 5-8%, respectively.

In terms of hydrophobic test surfaces, a notable enhancement in CHF was also observed on test surfaces. The CHF was improved by the anisotropic wicking surfaces (i.e., the averaged-deflected angle of pillars was 30°) by 23-28%. In contrast, the influence of vertical pillar arrays on boiling heat transfer was insignificant. Notably, the anisotropic wicking surfaces revealed a remarkable improvement in CHF compared to those surfaces comprised of vertical pillar arrays with the same spacing, by 21% and 23% as the center-to-center spacing between two neighboring pillars were 250 um and 500 um, respectively, as shown in Fig. 6(b). The

experimental observations indicated that the boiling heat transfer under subcooled conditions could be improved using the anisotropic wicking surfaces (i.e., surfaces composed of bending pillar arrays), which resulted in the anisotropic wicking behavior to improve the liquid replenishment capacity on heated surfaces along the flow direction.

Additionally, the HTC improvements of the hydrophilic-polymerized pillar surfaces (22.4-23.4 kW/m^2·K for 250-um center-to-center spacing; 18.7-20.2 kW/m^2·K for 500-um center-to-center spacing) were observed compared to the hydrophilic bare PDMS surface (14.2 kW/m^2·K), respectively. The increasing trend of improvements in HTC was also observed on the hydrophobic test surfaces with variation in spacings. Herein, HTC of surfaces composed of polymerized pillar arrays increased as the heat flux increased, specifically, as the vertical PDMS pillar arrays were varied to anisotropic wicking structures, i.e., the pillar arrays were deflected by depositing a thin gold layer on the one side of the polymerized pillars, as shown in Fig. 7.

Thus, in addition to the surface wettability, the enhancement in both CHF and HTC on the various-polymerized test surfaces can be predominantly referred to as the influence of center-to-center spacing between the polymerized pillars as well as the bending effect of pillar arrays associated with anisotropic wicking behavior.

3.2 Bubble characteristics on the hydrophilic anisotropic wicking surfaces

Bubble characteristics on the various hydrophilic test surfaces were shown in Fig. 8(a) and (b), in terms of the equilibrium diameter of a single-departing bubble as a function of the heat flux and the relationship between the release frequency of bubbles and the heat flux. According to the results of bubble visualization, however, the bubble characteristics on heated surfaces under subcooled flow boiling differed on those surfaces in saturated conditions where bubbles vanished rapidly before departing from the heated surfaces, owing to the dramatical decrease in the temperature gradient between condensation layer and layers consisted of evaporative microlayer and superheated layer [31]. In addition, bubble characteristics were significantly affected by the bubble lift force of the convective flow. The bubble coalescence becomes more vigorously at high heat flux during downstream regions along the flow direction; therefore, the bubble detachment characteristics in terms of the detachment diameter and the departure frequency of a single-departing bubble were recorded in a fixed region, where the width and the length were 1.5 mm and 2 mm, respectively [24].

We selected the surfaces composed of hydrophilic pillar arrays as the representative cases

for analyzing the influence of the bending effect of pillar arrays of anisotropic wicking surfaces on bubble characteristics. Among the hydrophilic test surfaces, the surface with polymerized pillar arrays showed the smallest bubble detachment diameter, which let bubbles released frequently from heated surfaces compared to the bare PDMS surface. Additionally, narrowing the center-to-center spacing between the polymerized pillars from 500 um to 250 um apparently reduced the size of departing bubbles accompanying the high bubble release frequency. These bubble characteristics were attributed to the active bubble nucleation sites and the augmentation of interfacial capillary flow between the pillar arrays [17].

Moreover, the anisotropic wicking surfaces with the same center-to-center spacings were released in a relatively small size in diameter of departing bubbles, which accelerated the bubble departure frequency, compared to bubbles that form on the surfaces comprised of vertical pillar arrays. As stated above, both the bending effect of the polymerized pillar arrays in terms of the anisotropic wicking and the influence of spacings between two neighboring pillars dominate the subcooled flow boiling heat transfer.

Fig. 9 shows the bubble visualization of hydrophilic- and hydrophobic-test surfaces with variation in the spacings between pillar arrays, i.e., the surfaces composed of the bending pillar arrays, as the heat flux was at 100 W/cm^2. In terms of the hydrophilic surfaces, active bubble nucleation and frequent bubble detachment behavior were observed on the surfaces composed of bending pillar arrays with 250-um spacing compared to the other hydrophilic test surfaces. In contrast, the hydrophobic test surfaces were continuously covered by bubbles even the heat flux reached the CHF, where altogether departing bubbles were not found on the test surfaces during the experiment. Thus, it was conjectured that bubbles tended to form on the hydrophobic surfaces with relatively large size in diameter and trap easily by roughened surfaces, especially when the surfaces with high hydrophobicity, resulting in a sudden transition in CHF [32-33].

3.3 Temporal surface temperature for hydrophilic-anisotropic wicking surfaces at CHF

In attempted to examine the influence of bending pillar arrays of the test surfaces on the flow instability within a convectional channel, the temporal surface temperature at points 1, 2, and 4 of RTDs for the hydrophilic test surfaces including vertical- and bending-pillar arrays with 250-um and 500-um spacings were depicted in Fig. 10, respectively. All the experimental results were recorded when the heat flux reached the CHF on the heated surfaces. Standard deviation (ϵ) was utilized to represent the temporal temperature fluctuation index, where an intense temperature deviation was first occurred at point 4 of the RTDs for all the test surfaces,

by analyzing the temperature variation on the representative surfaces. In terms of surfaces composed of polymerized pillar arrays with 250-um spacings, the lowest standard deviation on the surface with bending pillar arrays was observed compared to the vertical pillar surface, indicating that flow instability can be suppressed using the anisotropic wicking surfaces, which maintained a stable liquid film to facilitate the film evaporation on heated surfaces. A similar trend of the temporal surface temperature was found on surfaces composed of polymerized pillar arrays with 500-um spacing. The standard deviation on the anisotropic wicking surfaces was lower than the surfaces with vertical pillar arrays. These experimental observations indicated that the anisotropic wicking surfaces could be optimized to enhance the flow boiling heat transfer under subcooled conditions.

3.4 Bending effect of pillar arrays on wicking behavior on the anisotropic wicking surfaces

Wicking measurements were conducted on the hydrophilic test surfaces. The test samples' dimension was 5-mm in width and 10-mm in length, to determine the liquid supply capacity on the surfaces consisted of the polymerized pillar arrays including the vertical and bending pillars with 250-um and 500-um spacings, respectively. When the test surfaces reached the surface of the DI water, the bulk liquid flowed toward the top of the test surfaces owing to the capillary driving force occurred within the polymerized pillar arrays, which were recorded using a high-speed camera with a shutter rate of 6000 frame/s and a high power LED light source (100W) based on a shadowgraph method [23-24], as shown in Fig. 11(a). In addition, the liquid replenishment capacity on the test surfaces is associated with the relative wicking characteristics when the evaporation occurred on the heated surfaces, which indicated that a remarkable enhancement in subcooled flow boiling could be achieved on the surfaces showing the high capillary wicking. We quantified the wicking characteristics on test surfaces by estimating the averaged liquid propagation velocity, $W = l/t^{0.5}$where W is the wicking coefficient, l is the measured wicking distance, and t is the time of the bulk liquid propagation [34-35]. Among the vertical pillar surfaces, the wicking velocity showed on the surfaces with vertical polymerized pillar arrays with 250-um spacing (40.6 mm/s$^{0.5}$) was higher than those surfaces with 500-um spacing (18.9 mm/s$^{0.5}$); on the other hand, a significant improvement in the wicking characteristics was found on the surfaces with bending polymerized pillar arrays with 250-um (51.4 mm/s$^{0.5}$) and 500-um (26.8 mm/s$^{0.5}$) spacings, respectively. The experimental observations indicated that the liquid supply capacity on the test surfaces could be effectively improved using the surfaces consisting of the anisotropic wicking structures,

hence augmenting the overall subcooled flow boiling heat transfer performance.

Respecting the facts as mentioned above in terms of the bubble characteristics and the wicking behavior on the various test surfaces, when compared to the surfaces composed of vertical pillar arrays with the same center-to-center spacings (i.e., resulted in isotropic wicking behavior), using the anisotropic wicking surfaces not only improved the heat dissipation capacity through resulting in the relatively small departing bubbles, i.e., small vapor bubbles can be frequently released on the heated surfaces, but promising a stable liquid film within the pillar arrays, which effectively suppressed the flow instability, thus delaying the premature dry-out on the test surfaces, as shown in Fig. 12. Additionally, we inferred the enhancing mechanism of the wicking characteristics on the anisotropic wicking surfaces is associated with the anisotropic liquid spreading behavior on the test surfaces, which is discussed in the next section related to the relationship between liquid pinning forces induced by the polymerized pillar surfaces and the subcooled flow boiling.

3.5 Influence of liquid pinning force of the anisotropic wicking surfaces on subcooled flow boiling

In Fig. 13(a), once the droplet (5 μL) was deposited on the surfaces composed of polymerized pillar arrays, it spread along the bending direction of the pillars, resulting in the anisotropic wicking behavior. The liquid pinning force (F_r) on the polymerized pillar surfaces was evaluated based on previous works [36,37], by measuring the dynamic CAs, i.e., advancing (α)- and receding (β)-contact angles of the droplet, on the test surfaces, respectively. As time goes by, the droplet placed on the test surfaces stopped propagation because the liquid pinning force acting at the droplet's receding side was more considerable than forces that driven liquid toward the spreading direction. Herein we measured the dynamic CAs of the droplet on the pillar surfaces at an incipient point where the droplet started to spread along the test surfaces, for preventing an overprediction of the liquid pinning force; the measured results related to the dynamic CAs α and β on the various pillar surfaces were evaluated using the contact angle goniometer measurement with the photos recorded based on the shadowgraph method, were summarized in supplementary materials.

In addition, the liquid pinning force was estimated using correlations given by

$$F_p = \pi \cdot r \cdot \sigma[\cos\theta_r - \cos\theta_a] = \pi \cdot r \cdot \sigma[\cos\theta_r - \cos(\Delta\theta + \theta_r)] \quad (6)$$

where r is the radius of the contact line, σ is the surface tension of the DI water, θ_a and θ_r are the advancing- and receding- CAs, and $\Delta\theta$ is contact angle hysteresis (θ_a-θ_r), respectively.

Thus, the pinning force on the pillar surfaces were determined by substituting each parameter (r = 2mm, σ = 66.2 N/m, and the relative measured dynamic contact angels of the droplet) into Eq. (6), accordingly.

Fig. 13(b) shows the relationship between the liquid pinning force and the relative receding CAs measured on the surfaces composed of the hydrophilic- and hydrophobic-polymerized pillar arrays with 250-um and 500-um spacings, respectively. The liquid pinning force is proportional to the receding CAs on the various test surfaces, which corresponded to the experimental results proposed by [38]. On the other hand, the overall liquid pinning force on the hydrophilic-polymerized pillar surfaces was lower than the hydrophobic pillar surfaces, indicating that the liquid replenishment capacity could be further improved by manipulating the surface wettability of the anisotropic wicking surfaces. In addition, the anisotropic wicking surfaces with 250-um spacing showed the lowest liquid pinning force either for the hydrophilic or the hydrophobic surfaces, compared to those surfaces with 500-um spacing, indicating that the anisotropic liquid spreading behavior could be augmented by narrowing the center-to-center spacing between the pillar arrays. Moreover, in terms of the surfaces with the same spacings, the liquid pinning force on the vertical pillar surfaces decreased by deflecting the polymerized pillars where the liquid was spreading toward the pillar arrays' bending direction. These results showed a well-agreement with the previous discussion that the wicking characteristics on the surfaces composed of vertical polymerized pillar arrays could be improved using the surfaces with the anisotropic wicking structures.

Interestingly, the subcooled flow boiling heat transfer showed a strong dependence on the liquid pinning force acting on the surfaces comprised of polymerized pillar arrays with variation in the center-to-center spacings in Fig. 14. Accordingly, intensifying the surface wettability on the test surfaces significantly diminished the liquid pinning force on the test surfaces, i.e., increasing the liquid supply capacity, following the extension of the boiling crisis (CHF). Meanwhile, narrowing the center-to-center spacings between two neighboring pillars on the test surfaces resulted in enhanced CHF enhancement by strengthening the capillary driving forces within the polymerized pillar arrays. Moreover, changing the configuration of the vertical-polymerized pillar arrays into the anisotropic wicking surfaces with the bending pillar arrays effectively reduced the liquid replenishment resistance on the test surfaces, preventing the premature dry-out occurrence. Therefore, the boiling heat transfer in terms of the CHF under subcooled conditions were significantly dominated by the relative liquid pinning force on the various test surfaces. However, the hydrophilic surfaces consisted of the

bending pillar arrays with 250-um spacing was the optimal case for approaching high CHF and HTC among the polymerized test surfaces in this study.

4. Conclusions

This study experimentally investigated the influence of the anisotropic wicking surfaces with the bending pillar arrays on forced convective boiling heat transfer under subcooled conditions; PDMS materials were used to fabricate the vertical- and bending-pillar arrays with variation in the spacings (250-um and 500-um) between the pillars based on the method of the replica modeling.

The working fluid was DI water, i.e., the inlet temperature was maintained at 59.3±0.4°C, and the Re was 3600. Our findings, including the effects of the surface wettability, variation of the center-to-center spacing, and the configurations of the polymerized pillars (vertical and bending alignment) on the subcooled flow boiling heat transfer, are summarized below.

1. Among the test surfaces, hydrophilic surfaces composed of the polymerized pillar arrays with variation in the spacings between the pillars showed notable enhancements in CHF (17-34%) and HTC (32-71%) compared to the bare PDMS surfaces. These enhancements in boiling heat transfer were also observed on the hydrophobic test surfaces where the CHF and HTC were improved compared to the hydrophobic bare PDMS surface by 23-28% and 8-30%, respectively.
2. Compared to the vertical-polymerized pillar surfaces, the anisotropic wicking surfaces increased the capillary wicking by driving bulk liquid toward the bending direction of the polymerized pillars, which strengthened the averaged wicking velocity and subsequently maintained a stable liquid film on heated surfaces during the evaporation process, thus preventing the sudden transition of CHF.
3. Vapor bubbles form on the anisotropic wicking surfaces (bending-polymerized pillar arrays with the averaged tilted angle of 30°) revealed in the relatively small averaged detachment diameter as well as the high departure frequency compared to those vertical-polymerized pillar surfaces. Narrowing the center-to-center between the polymerized pillar arrays (from 500-um to 250-um) promoted bubble nucleation by resulting in large numbers of bubbles with a relatively small diameter, showing that the configuration of the polymerized pillars dominated the bubble characteristics.
4. Bubbles trapped on heated surfaces were observed on the surfaces composed of bending-polymerized pillar arrays with 250-um and 500-um spacings, respectively, even the heat flux reached the CHF, owing to the roughened surface with the strong

surface hydrophobicity, deteriorating the overall flow boiling heat transfer performance under subcooled conditions.

5. The influence of the anisotropic wicking surfaces of subcooled flow boiling was experimentally determined by analyzing the relationship between the liquid pinning force for the various polymerized pillar surfaces and the relative boiling heat transfer characteristics. The experimental results of this study could be used as the design criterion for optimizing the anisotropic wicking surfaces in subcooled flow boiling, accordingly.

Acknowledgement

This work was supported by the Human Resources Development program (No.20204030200110) of the Korea Institute of Energy Technology Evaluation and Planning(KETEP) grant funded by the Korea government Ministry of Trade, Industry and Energy.

Declaration of Competing Interest

The authors declare no competing financial interest.

References

[1] Nasri, M. & Dickinson, D. Thermal Management of Fuel Cell-driven Vehicles using HT-PEM and Hydrogen Storage. 6 (2014).

[2] Suzuki, K., Yuki, K. & Mochizuki, M. Application of Boiling Heat Transfer to High-Heat-Flux Cooling Technology in Power Electronics. *Transactions of The Japan Institute of Electronics Packaging* **4**, 127–133 (2011).

[3] Suzuki, K. & Inagaki, R. A Fundamental Study on High Heat Flux Cooling using Subcooled Flow Boiling with Microbubble Emission. 5 (2006).

[4] Suzuki, K. High heat flux transport by microbubble emission boiling. *Microgravity Sci. Technol* **19**, 148–150 (2007).

[5] Lee, W.-R. & Lee, J.-Y. Effect of Flow Instability on Pool Boiling and CHF of Thin Flat Plate Heater PCB. *Heat Transfer Engineering* **36**, 1028–1036 (2015).

[6] Li, C. *et al.* Nanostructured Copper Interfaces for Enhanced Boiling. *Small* **4**, 1084–1088 (2008).

[7] Morshed, A. K. M. M., Paul, T. C. & Khan, J. Effect of Cu-Al2O3 nanocomposite coating on flow boiling performance of a microchannel. *Applied Thermal Engineering* **51**, 1135–1143 (2013).

[8] Chen, R. *et al.* Nanowires for Enhanced Boiling Heat Transfer. *Nano Lett.* **9**, 548–553 (2009).

[9] Dong, L., Quan, X. & Cheng, P. An experimental investigation of enhanced pool boiling heat transfer from surfaces with micro/nano-structures. *International Journal of Heat and Mass Transfer* **71**, 189–196 (2014).

[10] Lee, D., Lee, N., Hsu, W.-T., Yun, M. & Cho, H. H. Enhanced boiling heat transfer on micro-structured surfaces via ultrasonic actuation. *International Communications in Heat and Mass Transfer* **113**, 104512 (2020).

[11] Shin, S., Choi, G., Kim, B. S. & Cho, H. H. Flow boiling heat transfer on nanowire-coated surfaces with highly wetting liquid. *Energy* **76**, 428–435 (2014).

[12] Morshed, A. K. M. M., Yang, F., Yakut Ali, M., Khan, J. A. & Li, C. Enhanced flow boiling in a microchannel with integration of nanowires. *Applied Thermal Engineering* **32**, 68–75 (2012).

[13] Li, D. *et al.* Enhancing Flow Boiling Heat Transfer in Microchannels for Thermal Management with Monolithically-Integrated Silicon Nanowires. *Nano Lett.* **12**, 3385–3390 (2012).

[14] Wang, S., Chen, H.-H. & Chen, C.-L. Enhanced flow boiling in silicon nanowire-coated manifold microchannels. *Applied Thermal Engineering* **149**, 1042–1057 (2019).

[15] Chu, K.-H., Soo Joung, Y., Enright, R., Buie, C. R. & Wang, E. N. Hierarchically structured surfaces for boiling critical heat flux enhancement. *Appl. Phys. Lett.* **102**, 151602 (2013).

[16] Shojaeian, M. & Koşar, A. Pool boiling and flow boiling on micro- and nanostructured surfaces. *Experimental Thermal and Fluid Science* **63**, 45–73 (2015).

[17] Zhu, Y. *et al.* Surface Structure Enhanced Microchannel Flow Boiling. *Journal of Heat Transfer* **138**, 091501 (2016).

[18] Chu, K.-H., Xiao, R. & Wang, E. N. Uni-directional liquid spreading on asymmetric nanostructured surfaces. *Nature Materials* **9**, 413–417 (2010).

[19] Chen, C.-M., Chiang, C.-L. & Yang, S. Programming Tilting Angles in Shape Memory Polymer Janus Pillar Arrays with Unidirectional Wetting against the Tilting Direction. *Langmuir* **31**, 9523–9526 (2015).

[20] Malvadkar, N. A., Hancock, M. J., Sekeroglu, K., Dressick, W. J. & Demirel, M. C. An engineered anisotropic nanofilm with unidirectional wetting properties. *Nature Materials* **9**, 1023–1028 (2010).

[21] Jokinen, V. Directional imbibition on a chemically patterned silicon micropillar array. *Soft Matter* **12**, 1100–1106 (2016).

[22] Kim, B. S. *et al.* Stable and uniform heat dissipation by nucleate-catalytic nanowires for boiling heat transfer. *International Journal of Heat and Mass Transfer* **70**, 23–32 (2014).

[23] Lee, D., Lee, N., Shim, D. I., Kim, B. S. & Cho, H. H. Enhancing thermal stability and uniformity in boiling heat transfer using micro-nano hybrid surfaces (MNHS). *Applied Thermal Engineering* **130**, 710–721 (2018).

[24] Hsu, W.-T., Lee, D., Lee, N., Yun, M. & Cho, H. H. Enhancement of flow boiling heat transfer using heterogeneous wettability patterned surfaces with varying inter-spacing. *International Journal of Heat and Mass Transfer* **164**, 120506 (2021).

[25] Chandra, D., Taylor, J. A. & Yang, S. Replica molding of high-aspect-ratio (sub-)micron hydrogel pillar arrays and their stability in air and solvents. *Soft Matter* **4**, 979 (2008).

[26] Pan, S., Chen, M. & Wu, L. Fabrication of a flexible transparent superomniphobic polydimethylsiloxane surface with a micropillar array. *RSC Adv.* **9**, 26165–26171 (2019).

[27] Wenzel, R. N. RESISTANCE OF SOLID SURFACES TO WETTING BY WATER. *Ind. Eng. Chem.* **28**, 988–994 (1936).

[28] Cassie, A. B. D. & Baxter, S. Wettability of porous surfaces. *Trans. Faraday Soc.* **40**, 546–551 (1944).

[29] Chen, C.-M. & Yang, S. Directed Water Shedding on High-Aspect-Ratio Shape Memory Polymer Micropillar Arrays. *Advanced Materials* **26**, 1283–1288 (2014).

[30] R.J. Moffat, Contributions to the theory of single-sample uncertainty analysis, ASME J. Fluids Eng. 104 (1982), 250–258.

[31] Zhou, P., Huang, R., Huang, S., Zhang, Y. & Rao, X. Experimental investigation on bubble contact diameter and bubble departure diameter in horizontal subcooled flow boiling. *International Journal of Heat and Mass Transfer* **149**, 119105 (2020).

[32] Wang, X., Zhao, S., Wang, H. & Pan, T. Bubble formation on superhydrophobic-micropatterned copper surfaces. *Applied Thermal Engineering* **35**, 112–119 (2012).

[33] Kim, J. M. *et al.* Effect of heterogeneous wetting surface characteristics on flow boiling performance. *International Journal of Heat and Fluid Flow* **70**, 141–151 (2018).

[34] Shim, D. I. *et al.* Enhancement of Pool Boiling Heat Transfer Using Aligned Silicon Nanowire Arrays. *ACS Appl. Mater. Interfaces* **9**, 17595–17602 (2017).

[35] Wen, R., Xu, S., Lee, Y.-C. & Yang, R. Capillary-driven liquid film boiling heat transfer on hybrid mesh wicking structures. *Nano Energy* **51**, 373–382 (2018).

[36] R, T. *et al.* Drop retention force as a function of resting time. *Langmuir* **24**, 9370–9374 (2008).

[37] Kim, T. & Suh, K. Y. Unidirectional wetting and spreading on stooped polymer nanohairs. *Soft Matter* **5**, 4131–4135 (2009).

Table Captions

Table 1 Details of the hydrophobic coating pattern design

Table 2 Uncertainties of the experimental variables

Table 1 Detail design information of the polymerized test surfaces

Surface wettability	Structures	Center-to-center spacing [um]	Averaged tilting angle [°]	Diameter [um]	Height [um]
Hydrophobic	Vertical	250	30	50	300
Hydrophobic	Vertical	500	30	50	300
Hydrophobic	Bending	250	30	50	300
Hydrophobic	Bending	500	30	50	300
Hydrophilic	Vertical	250	30	50	300
Hydrophilic	Vertical	500	30	50	300
Hydrophilic	Bending	250	30	50	300
Hydrophilic	Bending	500	30	50	300

Table 2 Experimental measurement uncertainties

Parameters	Uncertainty
Temperature measurement [℃]	0.2℃
Heater power measurement	0.34%
L	0.22%
μ, ρ	1.5%
V_f	4.59%
Re	4.56%
q_{loss}	6.37%
$\dot{Q}$	6.46%
h	9.1%

Figure Captions

Figure 1 Schematic diagram showing the influences of anisotropic wicking structures, which include surface wettability and bending effects, on the subcooled flow boiling.

Figure 2 Experimental equipment. (a) Experimental facilities for subcooled flow boiling. (b) Resistance temperature detector (RTD) sensor. (c) Detail design information of test section.

Figure 3 Schematic diagram of polymerized pillars. (a) Fabrication process of polymerized test surfaces. (b) PDMS stamps on a silicon substrate. (c) Scanning electron microscope (SEM) images for surfaces consisted of vertical- and bending- pillar arrays with 250-um and 500-um spacing, respectively.

Figure 4 Multi-layers of (a) Hydrophilic- and (b) Hydrophobic-test surfaces. (c) Scanning electron microscope (SEM) images of anisotropic wicking surfaces showing surfaces consisted of 200-nm SiO_2-, gold-, and PDMS- layers on silicon substrates (550 um).

Figure 5 Surface contact angle on polymerized test surfaces. (b) Surface contact angle as a function of roughness factor on surfaces composed of vertical- and bending-pillar arrays including hydrophilic and hydrophobic surfaces, respectively.

Figure 6 Subcooled flow boiling characteristics. (a) Heat flux versus degrees of subcooling for various hydrophilic test surfaces. (b) Heat flux versus degrees of subcooling for various hydrophobic test surfaces.

Figure 7 Comparison of the HTC between the hydrophilic- and hydrophobic- surfaces composed of PDMS pillar arrays with 250-um and 500-um spacing and bare PDMS plains.

Figure 8 Bubble detachment characteristics for the hydrophilic PDMS surfaces at Re=3600. (a) Bubble departure diameter as a function of the relative heat flux. (b) Bubble detachment frequency as a function of the relative heat flux.

Figure 9 Bubble detachment from (a) hydrophilic- and (b) hydrophobic PDMS surfaces including plains surfaces comprised of bending pillar arrays with 250-um and 500-um spacing, with heat flux of 100 W/cm^2, respectively.

Figure 10 Temporal surface temperature for hydrophilic PDMS surfaces at various points of RTD sensor. (a) vertical- and (b) bending-pillars with 500-um spacing and (c) vertical- and (d) bending-pillars with 250-um spacing.

Figure 11 Liquid supply capability of various-hydrophilic PDMS surfaces. (a) Surfaces composed of vertical- and bending- pillar arrays with 250-um and 500-um spacing, respectively. (b) Relationship between wicking length and time $t^{0.5}$ for PDMS pillar surfaces in vertical and bending alignment with inter spacing of 250-um and 500-um, respectively.

Figure 12 Schematic diagram showing the bending effects of PDMS pillars on liquid pinning force against the flow direction of cooling liquid in terms of subcooled flow boiling.

Figure 13 (a) Measurement of dynamic contact angle of droplet on surfaces composed of bending pillar arrays with 250-um spacing. (b) Liquid pinning force as a function of receding contact angle on various PDMS pillar surfaces.

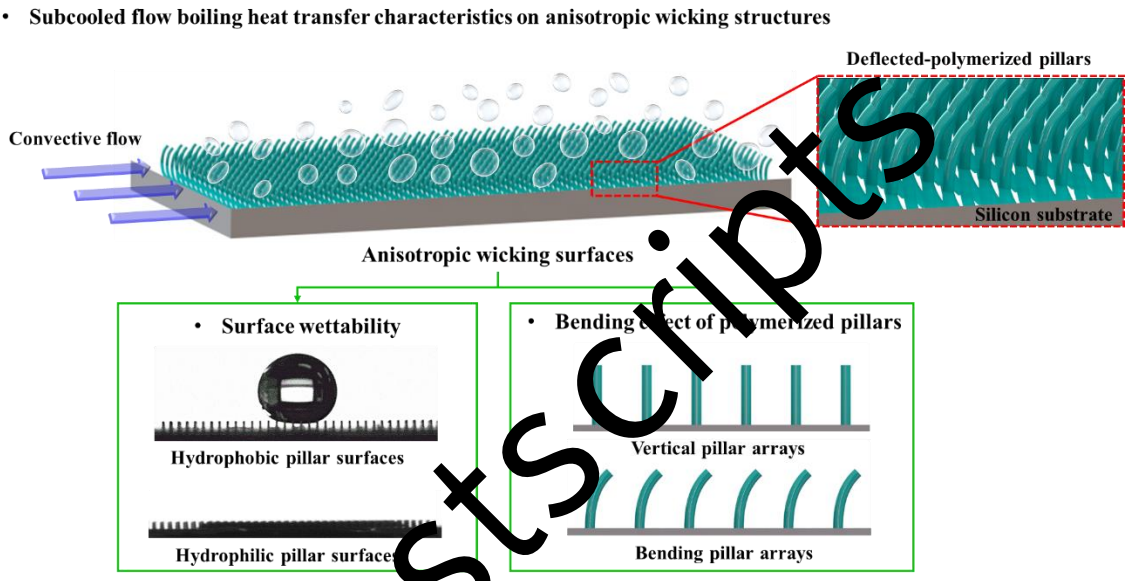

Fig. 1 Schematic diagram showing the influences of anisotropic wicking structures, which include surface wettability and bending effects, on the subcooled flow boiling.

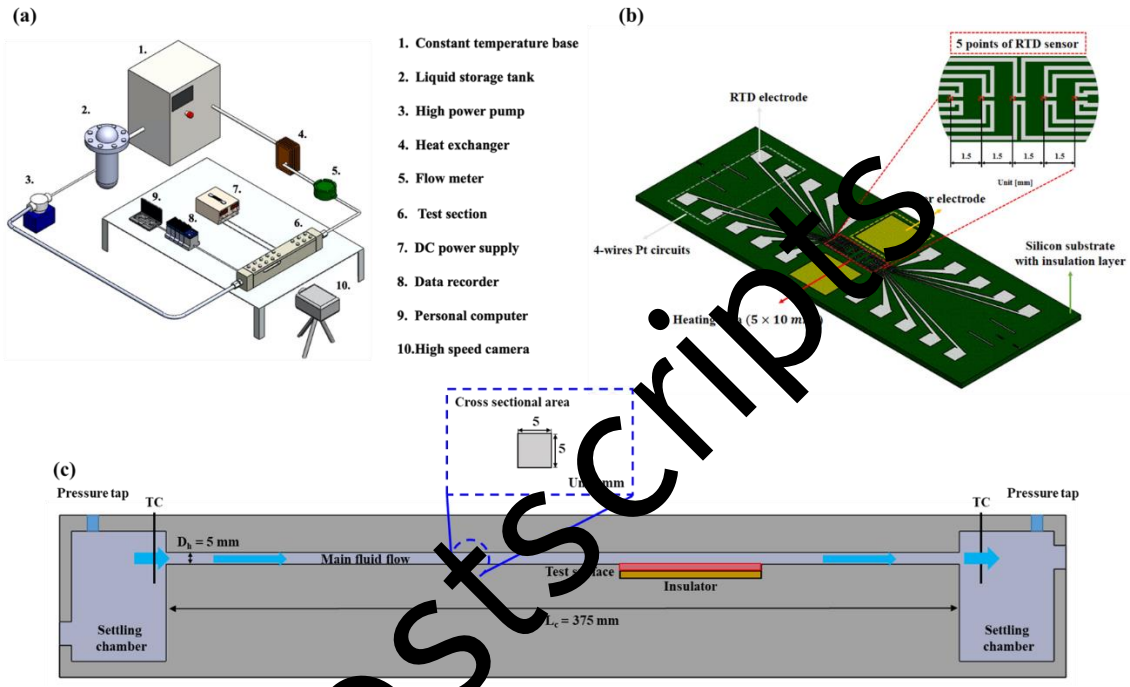

Fig. 2 Experimental equipment. (a) Experimental facilities for subcooled flow boiling. (b) Resistance temperature detector (RTD) sensor. (c) Detail design information of test section.

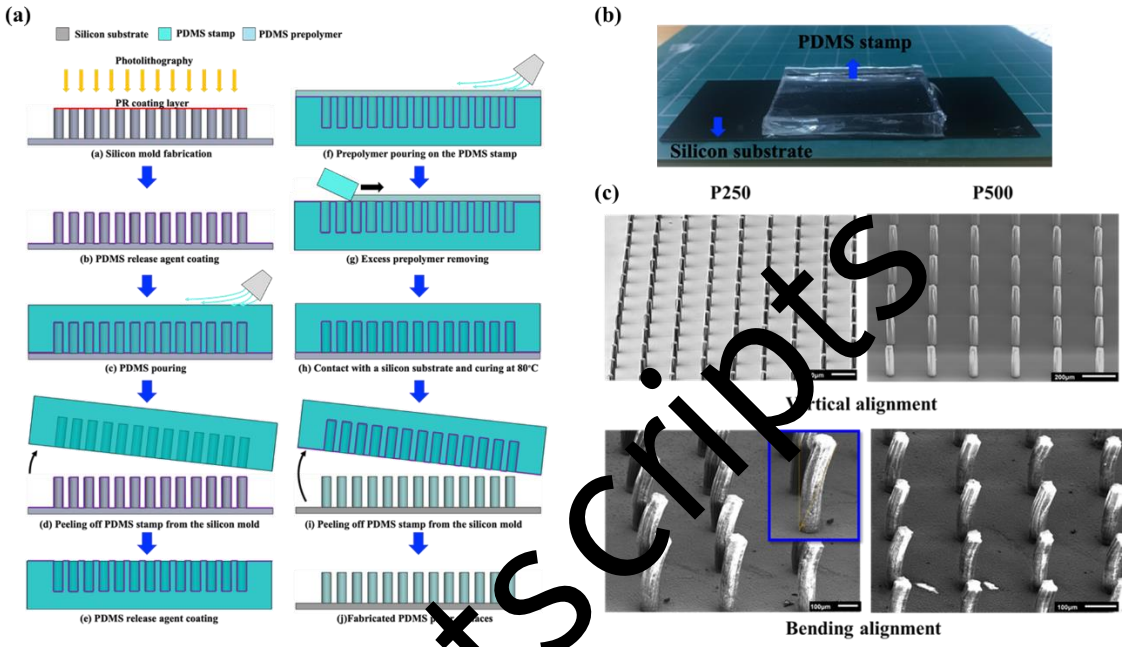

Fig. 3 Schematic diagram of polymerized pillars. (a) Fabrication process of polymerized test surfaces. (b) PDMS stamps on a silicon substrate. (c) Scanning electron microscope (SEM) images for surfaces consisted of vertical- and bending- pillar arrays with 250-um and 500-um spacing, respectively

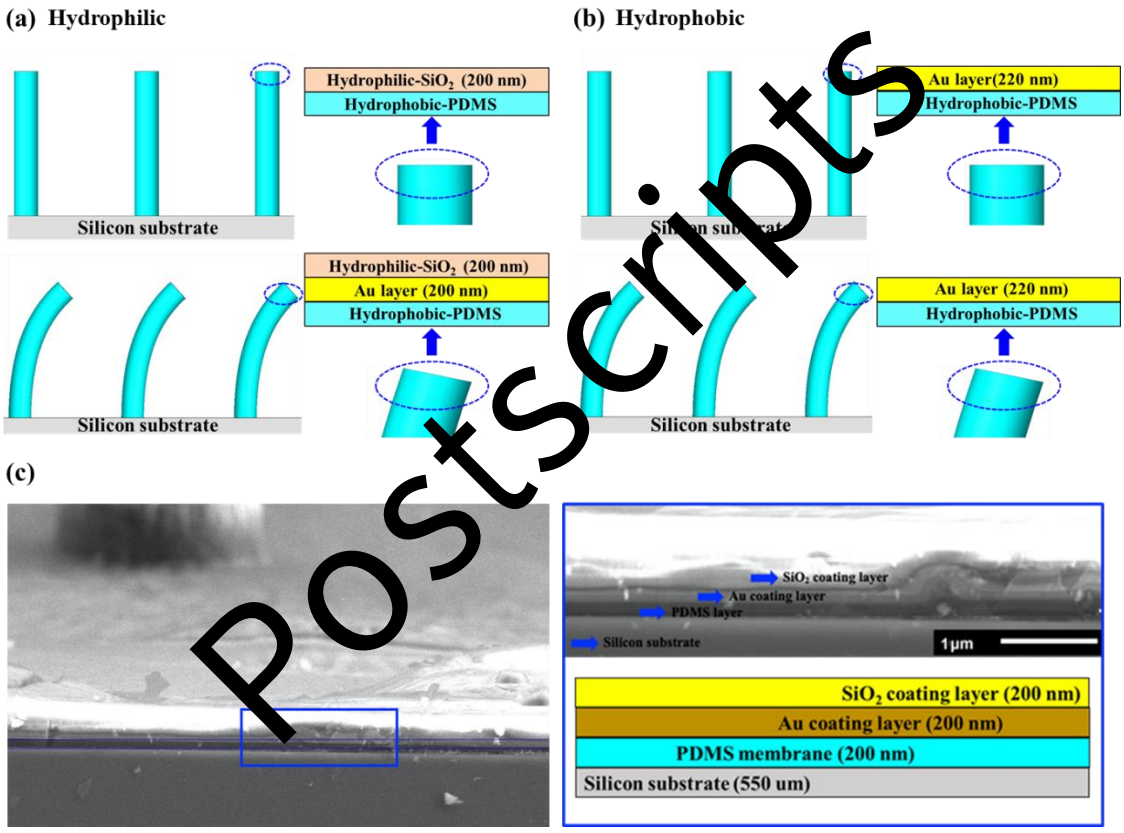

Fig. 4 Multi-layers of (a) Hydrophilic- and (b) Hydrophobic-test surfaces. (c) Scanning electron microscope (SEM) images of anisotropic wicking surfaces showing surfaces consisted of 200-nm SiO_2-, gold-, and PDMS- layers on silicon substrates (550 um).

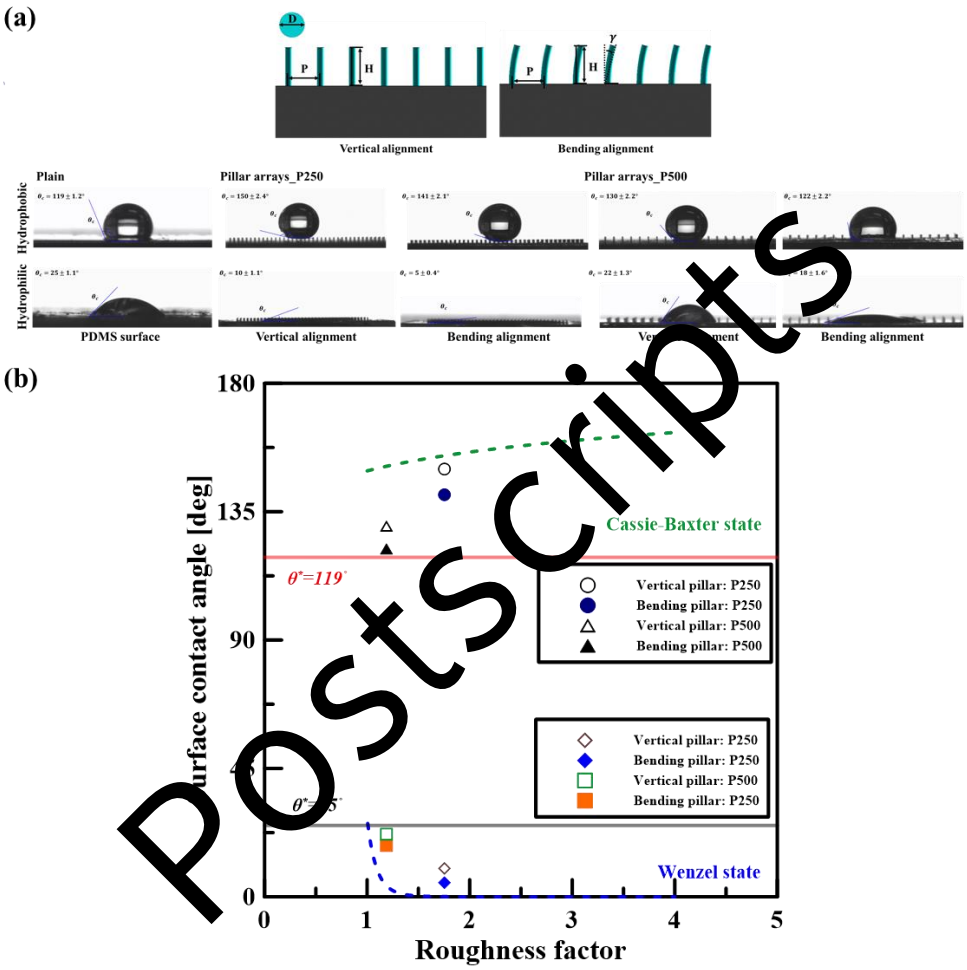

Fig. 5 (a) Surface contact angle on polymerized test surfaces. (b) Surface contact angle as a function of roughness factor on surfaces composed of vertical- and bending- pillar arrays including hydrophilic and hydrophobic surfaces, respectively.

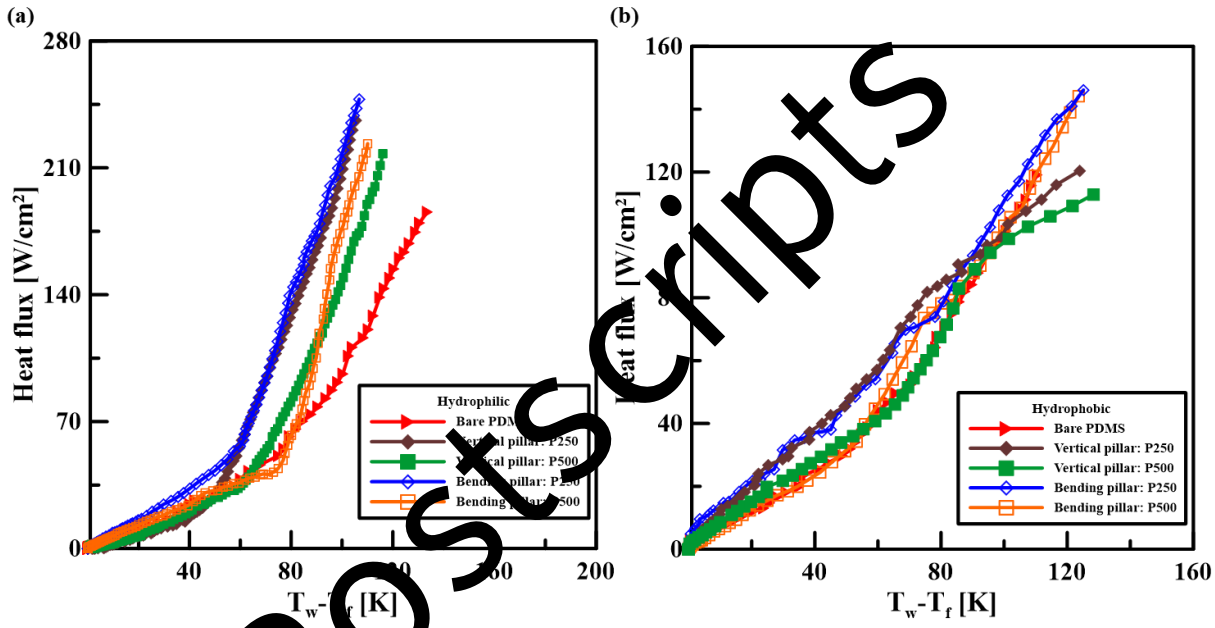

Fig. 6 Subcooled flow boiling characteristics. (a) Heat flux versus degrees of subcooling for various hydrophilic test surfaces. (b) Heat flux versus degrees of subcooling for various hydrophobic test surfaces.

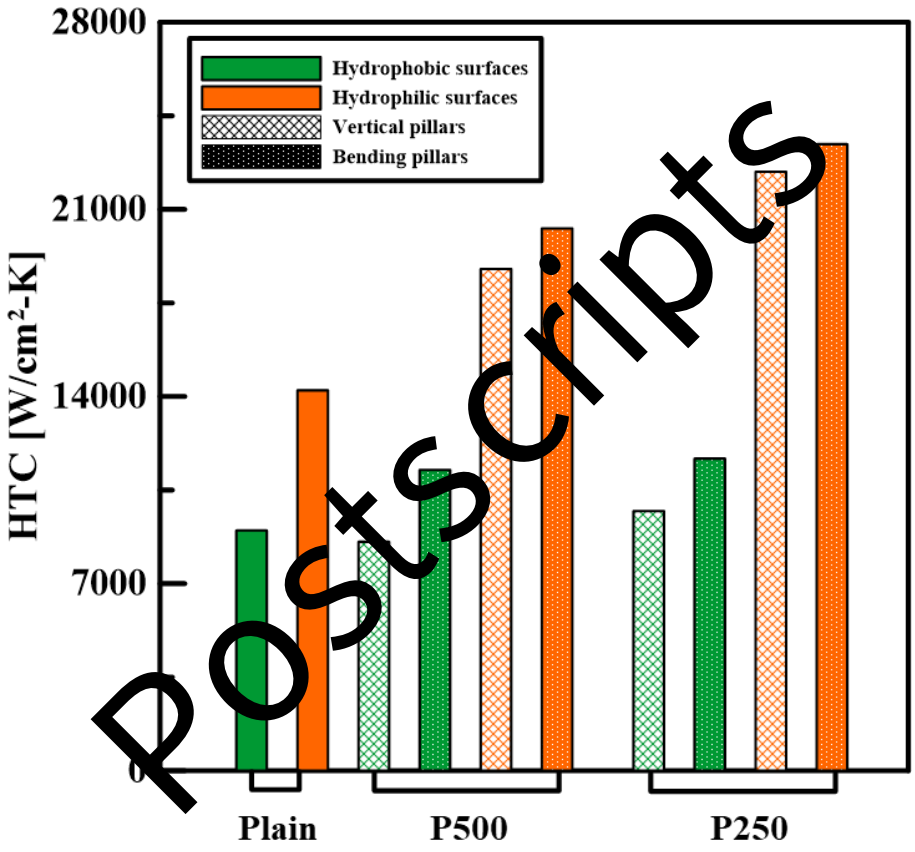

Fig. 7 Comparison of the HTC between the hydrophilic- and hydrophobic- surfaces composed of PDMS pillar arrays with 250-um and 500-um spacing and bare PDMS plains.

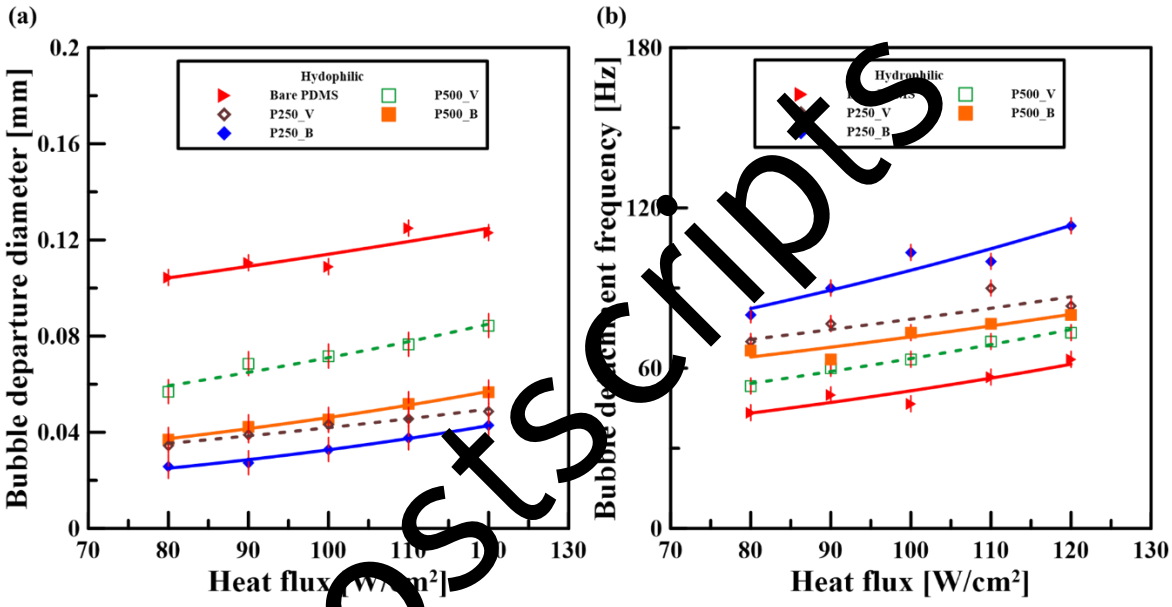

Fig. 8 Bubble detachment characteristics for the hydrophilic PDMS surfaces at Re=3600. (a) Bubble departure diameter as a function of the relative heat flux. (b) Bubble detachment frequency as a function of the relative heat flux.

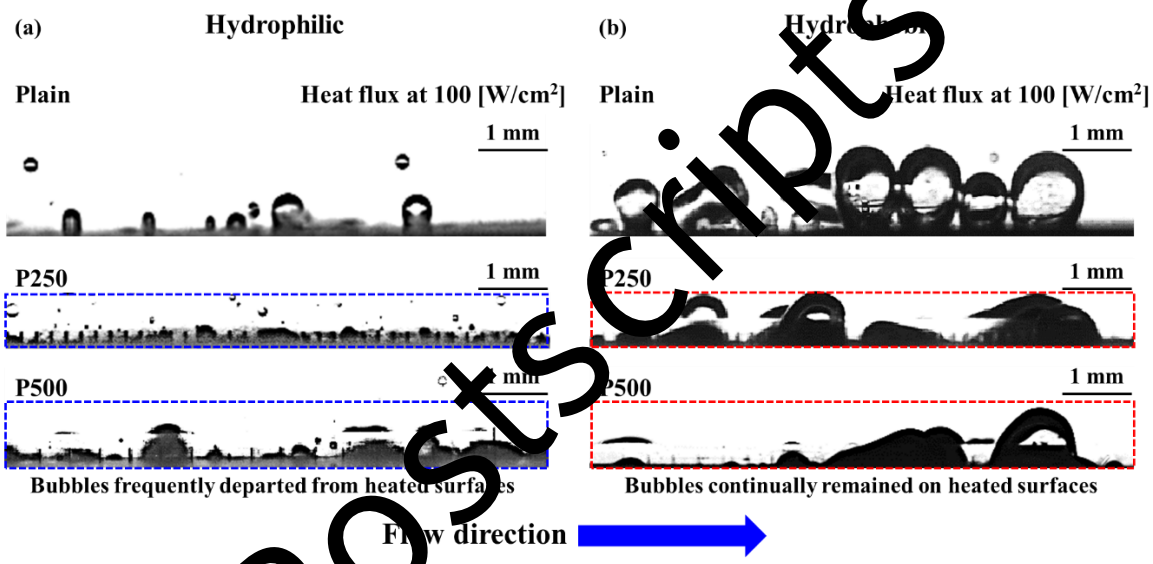

Fig. 9 Bubble detachment from (a) hydrophilic- and (b) hydrophobic PDMS surfaces including plains, surfaces comprised of bending pillar arrays with 250-um and 500-um spacing, with heat flux of 100 W/cm^2, respectively.

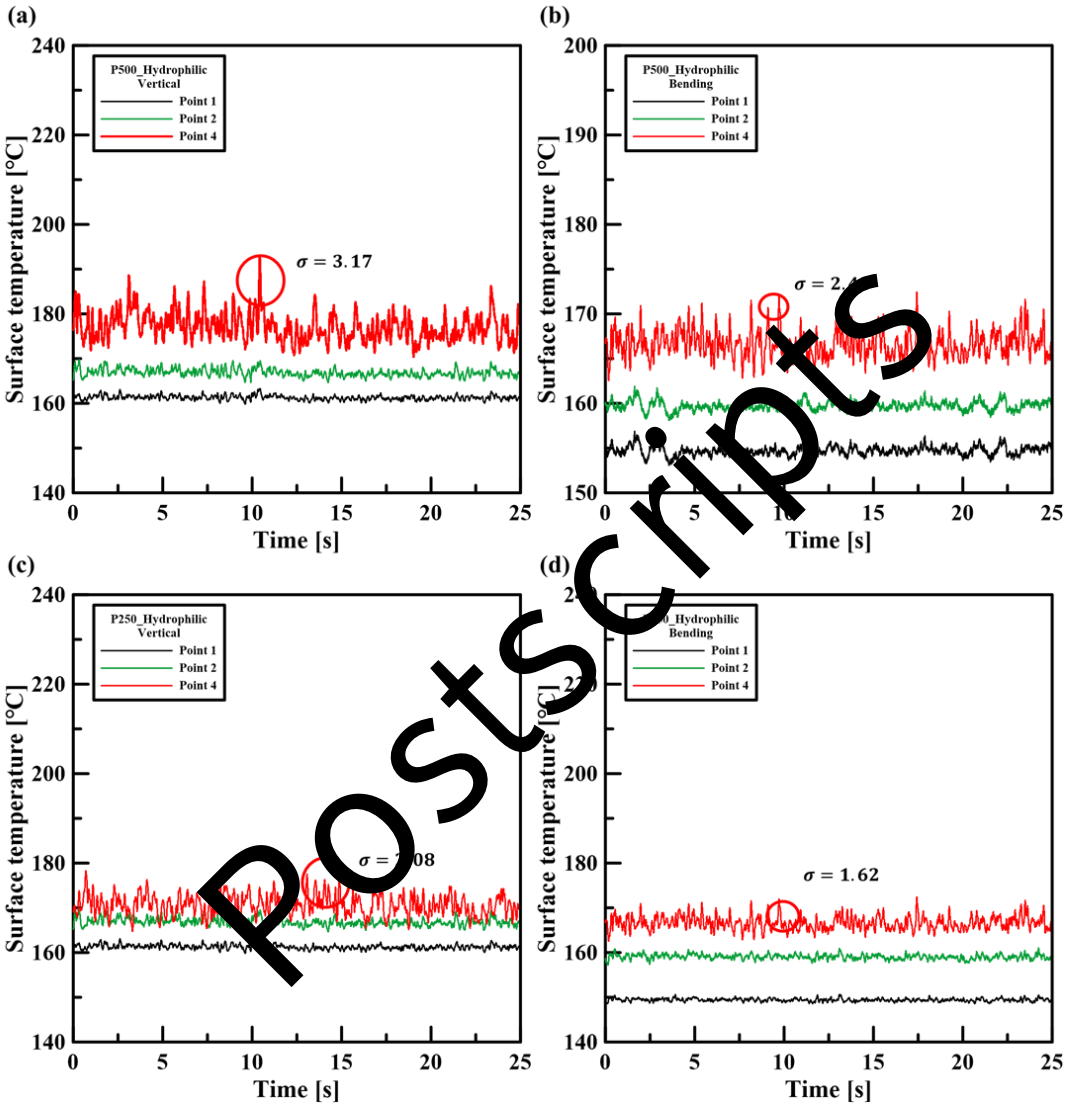

Fig. 10 Temporal surface temperature for hydrophilic PDMS surfaces at various points of RTD sensor. (a) vertical- and (b) bending-pillars with 500-um spacing and (c) vertical- and (d) bending-pillars with 250-um spacing.

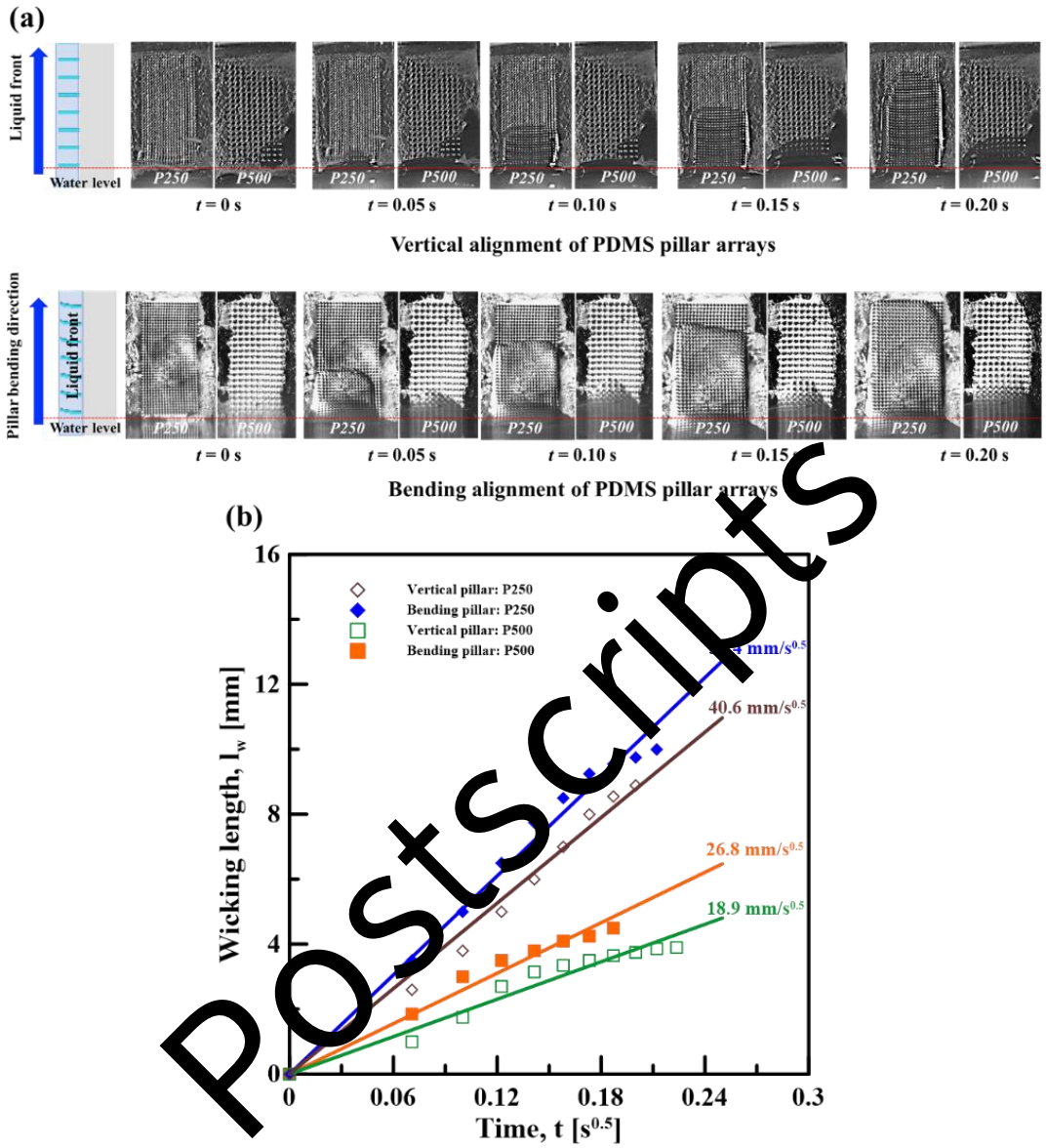

Fig. 11 Liquid supply capability of various-hydrophilic PDMS surfaces. (a) Surfaces composed of vertical- and bending- pillar arrays with 250-um and 500-um spacing, respectively. (b) Relationship between wicking length and time $t^{0.5}$ for PDMS pillar surfaces in vertical and bending alignment with inter spacing of 250-um and 500-um, respectively.

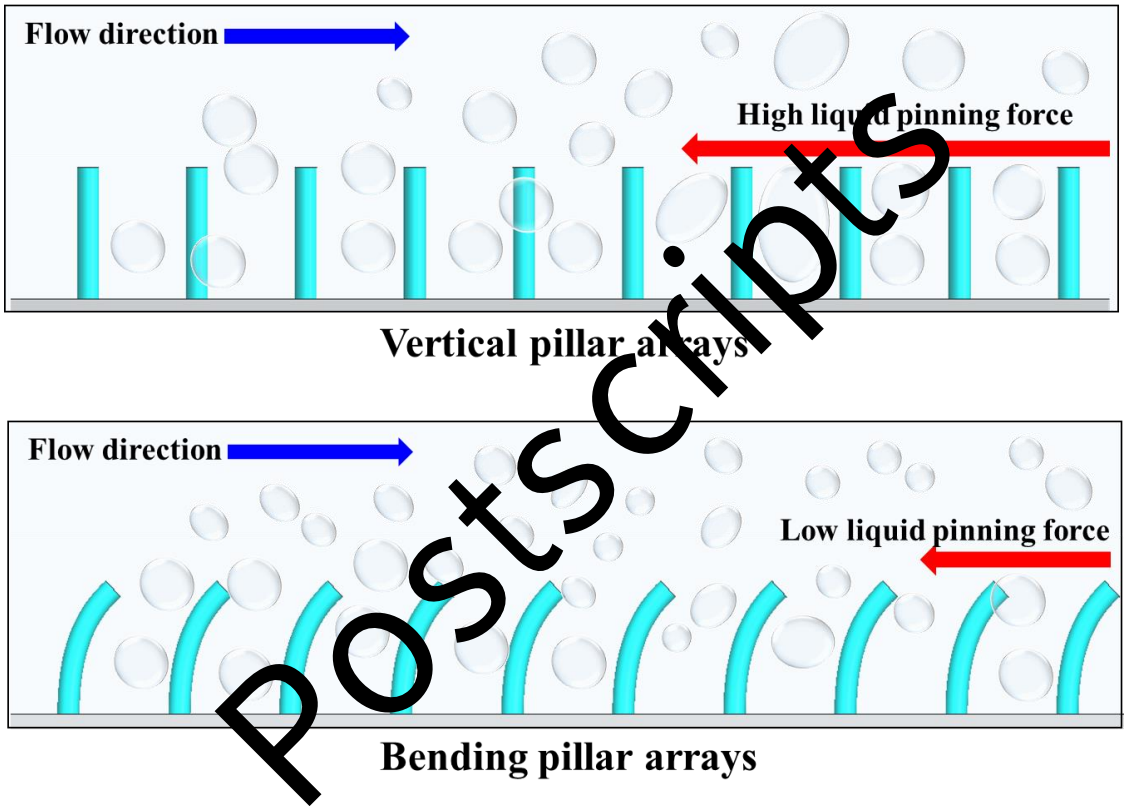

Fig. 12 Schematic diagram showing the bending effects of PDMS pillars on liquid pinning force against the flow direction of cooling liquid in terms of subcooled flow boiling.

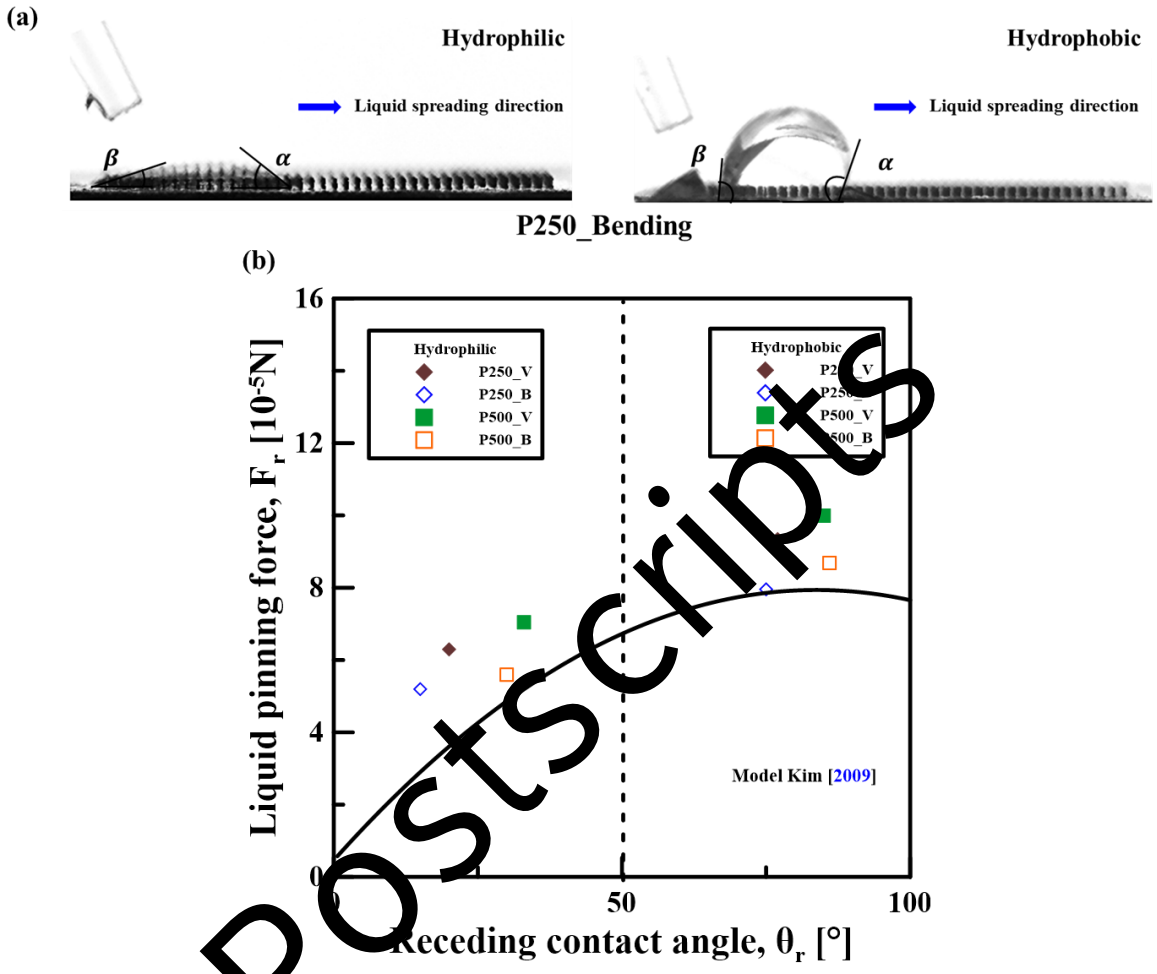

Fig. 13 (a) Measurement of dynamic contact angle of droplet on surfaces composed of bending pillar arrays with 250-um spacing. (b) Liquid pinning force as a function of receding contact angle on various PDMS pillar surfaces.

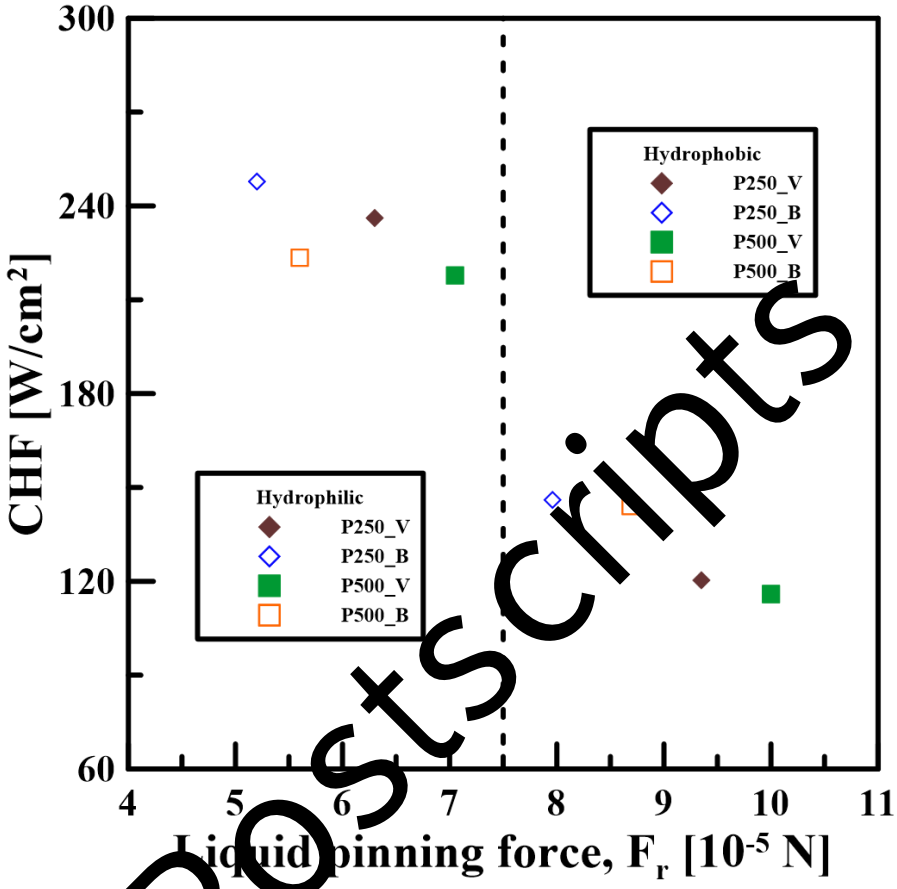

Fig. 14 Relationship between the CHT and liquid pinning forces for various PDMS surfaces including hydrophilic and hydrophobic surfaces, respectively.